energies

MDPI

Article

Investigation of the Effects of Ambient Conditions and Injection Strategies on Methanol Spray Characteristics

Decheng Wang [1,2], Wuzhe Zhu [3], Zhijie Li [1,2], Changhui Zhai [1,2], Xiaoxiao Zeng [1,2], Kui Shi [1,2], Yunliang Qi [3] and Zhi Wang [3,*]

[1] Weichai Power Co., Ltd., Weifang 261001, China; wangdc@weichai.com (D.W.); lizhij@weichai.com (Z.L.); zhaich@weichai.com (C.Z.); zengxx@weichai.com (X.Z.); shik@weichai.com (K.S.)
[2] State Key Laboratory of Engine and Powertrain System, Weifang 261001, China
[3] School of Vehicle and Mobility, Tsinghua University, Beijing 100084, China; zhuwz24@mails.tsinghua.edu.cn (W.Z.); qiyunliang@tsinghua.edu.cn (Y.Q.)
* Correspondence: wangzhi@tsinghua.edu.cn

Abstract

To reveal the physical evolution of methanol spray under different environmental conditions and injection strategies, this study focuses on the atomization and evaporation behavior of low-pressure methanol spray. The coupled effects of temperature, pressure, and injection parameters are systematically investigated based on constant-volume combustion chamber experiments and three-dimensional CFD simulations. The formation, evolution, and interaction mechanisms of the liquid column core and cooling core are revealed. The results indicate that temperature is the dominant factor influencing methanol spray atomization. When the temperature increases from 255 K to 333 K, the spray penetration distance increases by approximately 70%, accompanied by a pronounced shortening of the liquid-core length and enhanced evaporation and air entrainment. Under low-temperature conditions, a stable liquid-core structure and a strong cooling core are formed, characterized by a high-density, long-axis morphology and an extensive low-temperature region, which suppress fuel–air mixing and ignition. Increasing the ambient pressure improves spray–air mixing but reduces penetration; at 255 K, increasing the ambient pressure from 0.05 MPa to 0.2 MPa increases the spray cone angle by approximately 10% while reducing the penetration distance by about 50%. Furthermore, optimizing the injection pressure or shortening the injection pulse width effectively enhances atomization performance: increasing the injection pressure from 0.4 MPa to 0.6 MPa and reducing the pulse width from 5 ms to 2 ms increases the penetration distance by approximately 30% and reduces the mean droplet diameter by about 20%.

Keywords: methanol; spray characteristics; computational fluid dynamics; constant-volume chamber

Check for updates

Academic Editor: Marcin Dębowski

Received: 16 November 2025
Revised: 23 December 2025
Accepted: 11 January 2026
Published: 14 January 2026

Copyright: © 2026 by the authors. Licensee MDPI, Basel, Switzerland. This article is an open access article distributed under the terms and conditions of the Creative Commons Attribution (CC BY) license.

1. Introduction

Internal combustion engines (ICEs) constitute a major component in transportation, agricultural production, refrigeration systems, and power generation equipment. Although modern ICEs widely employ aftertreatment technologies to achieve exhaust purification, their dependence on fossil fuels still results in substantial emissions of greenhouse gases and harmful pollutants. In sectors where full electrification of powertrains remains challenging, renewable energy carriers such as methanol, ammonia and hydrogen are becoming key technical paths to address environmental concerns [1,2]. According to publicly available

statistics from Eurostat, the share of petroleum and petroleum products in energy use decreased from 88.7% in 2013 to 79.0% in 2023. In contrast, the share of renewable and biofuels increased from 11.3% to 18.4% over the same period, corresponding to an increase of approximately 63% [3]. Taking renewable methanol as an example, its advantages such as volumetric energy density, raw material universality, storage and transportation convenience, and mature preparation process are regarded as strategic carriers for low-carbon transformation [4,5]. In comparison with hydrogen and ammonia, methanol offers several notable advantages. Being a liquid fuel in ambient conditions, methanol can be readily stored, transported, and integrated into existing fuel infrastructures without requiring high-pressure containment or cryogenic technologies. Moreover, methanol has a comparatively higher volumetric energy density than hydrogen, making it more suitable for onboard fuel storage and extended driving range in vehicle applications.

Currently, methanol application in engines mainly involves two forms: port fuel injection (PFI) [6] and direct injection (DI) [7]. Among these, PFI offers advantages such as low injection pressure, simple nozzle structure, and low cost, making it widely adopted [1] in internal combustion engines. In the PFI approach, methanol is injected into the intake manifold, where a methanol–air mixture is formed during the intake and compression strokes, and this premixed charge enters the cylinder near top dead center for combustion. Therefore, the atomization and mixing characteristics of the fuel spray within the intake port are particularly critical for PFI engines. Compared with conventional diesel fuel, methanol significantly deteriorates the formation quality and combustion stability of the mixture at low ambient temperatures due to its high latent heat of vaporization (1100 kJ/kg), low boiling point (64.7 °C), and low volumetric energy density (16 MJ/L) [8].

At present, the application of methanol-fueled engines remains limited, and the scarcity of publicly available experimental data constrains further technological development. The accuracy of computational fluid dynamics (CFD) simulations in engine research and development relies heavily on the precision of fundamental spray parameters. Conventional diesel spray models cannot be directly applied to methanol systems due to the significant differences in their physicochemical properties, particularly the coupled effects of methanol's low volumetric energy density and high latent heat of vaporization. In existing literature, Wang et al. [9] conducted a systematic experimental investigation of high-pressure methanol spray characteristics in a constant-volume combustion chamber using schlieren imaging. The results showed that injection pressure, ambient temperature, and ambient pressure significantly affect spray penetration and cone angle. Moreover, methanol spray behavior exhibited good similarity to gas-jet models, providing key experimental evidence for calibrating high-pressure direct-injection (HPDI) methanol spray models. Furthermore, using diesel spray as a reference, Wang et al. [10] performed a comparative study on high-pressure direct-injection methanol-engine sprays by combining diffuse back-illumination extinction imaging (DBI) and schlieren diagnostics. They found that, due to methanol's low boiling point, high latent heat of vaporization, and low viscosity, methanol spray boundaries are more irregular, characterized by a shorter vapor-phase tip penetration and a larger cone angle. While the overall spray area is comparable to diesel, methanol exhibits smaller liquid-phase penetration and area and a higher overall evaporation rate. In spray prediction and modeling, Leng et al. [11] used high-speed photography to investigate high-pressure methanol spray behavior under varying injection pressure, injection duration, ambient pressure, and temperature. They developed both an empirical correlation model based on experimental data and a deep-learning-based prediction model, achieving high-accuracy predictions for key parameters such as spray penetration. For spray–wall interaction under port fuel injection (PFI) conditions, Zhang et al. [12] employed DBI together with refractive-index matching (RIM) to systematically study methanol spray

impingement and wall wetting. They quantified the effects of spray impingement distance, wall temperature, and injection pressure on spray morphology, impingement height/width, and wall fuel-film mass. The results indicated that increasing the impingement distance drives the spray shape transition from conical to columnar; higher injection pressure enhances post-impingement spray spreading; and higher wall temperature significantly reduces fuel-film mass. Under high-temperature conditions, a Leidenfrost-induced rebound of the liquid film was also observed. Regarding extreme conditions and phase-change atomization, Liu et al. [13] reported that increasing ambient pressure suppresses spray penetration while enlarging the spray cone angle, and that elevating methanol temperature to a critical value (e.g., 85 °C) can trigger flash-boiling, markedly increasing spray velocity. However, at high temperature the injector drive current may fluctuate, leading to injection delay. Li et al. [14] systematically studied flash-boiling characteristics of methanol sprays under extremely cold conditions and found that ambient temperature directly affects the onset time of complete spray collapse. Wu et al. [15] further examined the combined effects of sub-atmospheric pressure, spray concentration, ambient temperature, and injection pressure on methanol atomization and micro-explosion behavior, confirming that negative-pressure environments significantly accelerate the micro-explosion process. To reveal internal mechanisms of spray formation, Chen et al. [16] combined three-dimensional numerical simulations with experiments. In the simulations, a simplified injector model was established and a mixture multiphase flow model coupled with the Schnerr–Sauer cavitation model was applied to analyze methanol internal-flow behavior under different temperatures and injection pressures, accounting for temperature-dependent variations in saturated vapor pressure, viscosity, and density. Experimentally, a phase Doppler particle analyzer (PDPA) was used to measure the Sauter mean diameter (SMD) and droplet velocity distributions at different temperatures to validate the numerical results. In reactive and safety-related studies, Wu et al. [17] experimentally analyzed explosion characteristics and flame propagation of methanol sprays under negative-pressure environments. By varying injection pressure, spray concentration, and initial temperature, they examined the coupled relationship between atomization behavior and explosion metrics. The results showed that increasing injection pressure significantly enhances peak explosion pressure, pressure rise rate, and flame temperature, whereas excessively high methanol concentration suppresses explosion intensity. Increasing initial temperature reduces droplet size and markedly elevates explosion risk; when droplet diameter decreases below 10 μm, methanol spray explosions progressively resemble gas-phase methanol explosions. For combustion and emissions, Cui et al. [18] systematically investigated the impacts of flash-boiling atomization under direct injection on combustion and emissions in a constant-volume chamber. Using high-speed imaging, online FTIR gas analysis, and TEM characterization of soot morphology, they compared supercooled and flash-boiling sprays. The results indicated that flash-boiling significantly improves combustion efficiency under rich conditions, reduces unburned hydrocarbon emissions by about 30%, and substantially suppresses NOx, aromatics, and soot formation. Meanwhile, soot particles formed under flash-boiling conditions are smaller with more compact graphitic-layer structures, indicating stronger resistance to oxidation. In addition, Chen et al. [19] visualized diesel/methanol dual direct-injection cross sprays and combustion, showing that diesel–methanol spray intersection and collision can strongly promote droplet interactions and mixture uniformity. Under flash-boiling conditions, larger axial and radial growth rates were observed; increasing injection pressure shortened ignition delay, reduced equivalence ratio, and suppressed soot formation, thereby improving dual-fuel combustion stability. In engineering-oriented and realistic-geometry investigations, Zhao et al. [20] studied methanol spray mixing, flame propagation, and hot-jet evolution inside a realistic visualized active pre-chamber (APC),

using Mie scattering and flame chemiluminescence imaging to assess the effects of injection pressure and injection duration. They found that methanol spray undergoes multiple wall impingements inside the confined APC, inducing tumble-like flows that enhance mixing. Although higher injection pressure accelerates spray penetration, it also increases bottom-wall liquid accumulation and is unfavorable for flame acceleration; geometric differences between the conical and tubular sections significantly affect flame propagation speed and jet morphology. Addressing intake cooling caused by methanol's high latent heat, Pu et al. [21] proposed a simplified yet physically consistent evaporation model that separately models droplet evaporation and wall-film evaporation for PFI methanol. The results show that droplet evaporation contributes marginally, while intake temperature reduction is dominated by wall-film evaporation; reducing initial droplet size or applying a co-flow injection angle is more effective than solely increasing intake temperature. Sun et al. [22] used large-eddy simulation (LES) with a reduced chemical mechanism to study methanol spray autoignition and combustion in a high-reactivity n-heptane environment. They reported that high-temperature and high-equivalence-ratio conditions significantly shorten methanol ignition delay and expand high-temperature reaction zones. As ambient temperature increases, the ignition location shifts from the mid-spray region to the leading edge, and the combustion mode transitions from reactivity-controlled to diffusion-controlled. The related studies have been systematically reviewed and summarized in Table 1.

Table 1. Comparative table of methanol studies in ICEs.

Study	Type	Application/Focus	Injection Method
Wang et al. [9]	Experimental	High-pressure methanol spray characterization in CVCC	HPDI
Wang et al. [10]	Experimental	Methanol vs. diesel spray comparison	HPDI
Leng et al. [11]	Experimental Modeling Machine learning	Spray penetration prediction and correlation development	DI
Zhang et al. [12]	Experimental	Spray–wall interaction and wall wetting under PFI	PFI
Liu et al. [13]	Experimental	Extreme conditions: ambient pressure effects and flash-boiling threshold	PFI
Li et al. [14]	Experimental	Flash-boiling under extremely cold conditions; spray collapse timing	DI
Wu et al. [15]	Experimental	Sub-atmospheric pressure effects; micro-explosion behavior	
Chen et al. [16]	Simulation Experimental validation	Internal nozzle flow, cavitation, and temperature-dependent properties; droplet sizing	DI
Wu et al. [17]	Experimental	Spray explosion and flame propagation under negative pressure	DI
Cui et al. [18]	Experimental	Flash-boiling effects on combustion and emissions in CVCC	DI
Chen et al. [19]	Experimental	Diesel/methanol dual DI cross-spray interaction and combustion	DI
Zhao et al. [20]	Experimental	Methanol spray mixing and flame/hot-jet evolution in active pre-chamber	DI
Pu et al. [21]	Simulation Modeling	Intake cooling mechanism: droplet vs. wall-film evaporation	PFI
Sun et al. [22]	Simulation	Methanol spray autoignition/combustion in high-reactivity environment	DI

Existing studies have substantially advanced the understanding of methanol sprays across high-pressure DI, PFI wall wetting, flash-boiling regimes, nozzle cavitation, and even combustion/safety behavior. Nevertheless, there is still a lack of systematic studies

on methanol spray characteristics suitable for low injection pressure (less than 1 MPa) and cold start conditions for PFI engines.

The present study aims to systematically explore the evolution mechanisms of methanol spray under different ambient temperatures, ambient pressures, and injection strategies in a constant-volume combustion chamber. Specifically, the objectives are to

(1) Quantitatively investigate the evolution characteristics of methanol spray under low-pressure and low-temperature conditions relevant to engine cold start, with particular emphasis on spray penetration, cone angle, and macroscopic spray morphology;
(2) Provide high-quality experimental data to support the calibration and validation of three-dimensional CFD models for methanol spray;
(3) Conduct a mechanistic analysis of low-pressure methanol spray development using three-dimensional numerical simulations on the CONVERGE platform, thereby providing a reliable design basis for improving engine cold-start performance and optimizing port fuel injection (PFI) systems.

2. Materials and Methods

2.1. Experimental Setup

In this study, spray characteristic tests were conducted in a constant-volume combustion chamber. The chamber has two 100 mm optical windows to provide optical access. Coolant circulation loops are installed on both the top and bottom surfaces, with a –60 °C cooling medium supplied for ambient temperature control. The fuel injector is mounted on the top of the chamber, and its fuel temperature is regulated through a circumferential coolant loop. Both the injector and the fuel supply system are equipped with temperature sensors and temperature control units for real-time monitoring and dynamic adjustment. The methanol injection pressure is provided by a nitrogen-driven gas–liquid booster pump. Nitrogen is the ambient gas, and a purging operation is performed inside the bomb after each test to eliminate residual exhaust gas interference with subsequent tests. An OMEGA DPG409-015A pressure sensor (OMEGA Engineering Inc., Norwalk, CT, USA) is installed in the chamber to monitor ambient pressure in real time. Spray visualization was performed using the direct imaging method. Figure 1a shows the experimental setup, which includes the methanol injection system, the high-speed imaging system, and the control system. Images were acquired using a Photron SA-Z high-speed camera (FASTCAM SA-Z, Photron Limited, Tokyo, Japan) with a frame rate of 10,000 fps, an image resolution of 1024 × 1024 pixels, a spatial resolution of 98.2 μm/pixel, and an exposure time of 10 μs. Therefore, the quantization uncertainty of length-based parameters (e.g., spray penetration) was estimated as ±1 pixel, corresponding to ±0.098 mm. The methanol nozzle used was a multi-hole type with 14 straight holes. The axis of each hole was parallel to the injector axis, and the diameter of each hole was 0.25 mm. Its appearance is shown in Figure 1b.

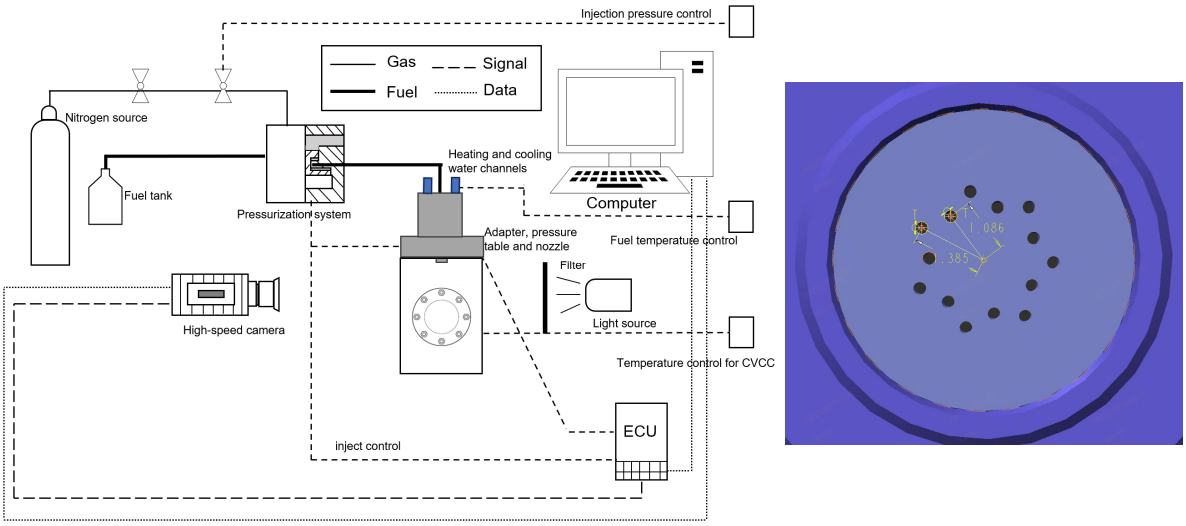


Figure 1. Experimental test bench and the nozzle shape (**a**) experimental test bench; (**b**) the nozzle shape.

2.2. Experimental Conditions

Table 2 lists the experimental conditions. These conditions are close to cold-start operating environments. Meanwhile, the influence of the injection strategy on the spray characteristics was also studied with injection pulse widths and the injection pressures. In this experiment, the uncertainty mainly stemmed from fluctuations in ambient conditions during testing, as well as from parameter extraction and data processing. Therefore, during the experiment, each condition was tested six times to ensure that the changes in temperature and pressure were within ±1 K and ±5%, respectively. When extracting spray parameters using image processing techniques, background subtraction combined with edge enhancement was applied to improve the stability of the results. Finally, the average value was used as the reported result, and the experimental uncertainties were represented using error bars, which are also shown in the results.

Table 2. Experimental conditions.

Parameter	Value
Ambient and fuel temperature (K)	255, 273, 293, 313, 333
Ambient pressure (MPa)	0.05, 0.1, 0.2
Injection pressure (MPa)	0.4, 0.6
Injection pulse width (ms)	2, 5

2.3. Data Processing

The spray parameters were extracted from the schlieren images using custom-written MATLAB code (MATLAB R2023a, MathWorks), as shown in Figure 2. The atomization images were binarized using a dynamic threshold segmentation technique, and the optimal segmentation threshold was automatically determined using the Otsu algorithm to perform edge feature extraction [23]. This threshold selection strategy is based on the principle of maximizing inter-class variance and can effectively distinguish the spray region from the background area. Its reliability has been validated in multiple studies on spray characterization [24] and is a key preprocessing step for extracting spray parameters from images. After binarization, the spray boundary was further processed to obtain the spray parameters. Spray parameters such as spray penetration distance (L), spray cone angle (θ), and spray area were calculated. To ensure consistency when comparing spray penetration lengths under different conditions, the penetration length was defined as the vertical distance from

the nozzle orifice to the farthest downstream spray edge. The spray width (d) was defined as the distance between the leftmost and rightmost edges of the spray. The spray area and cone angle were calculated as: $S = \frac{dL}{2}$, $\theta = 2\arctan\left(\frac{d}{2L}\right)$. For the processing of droplet diameter data, we select droplets with deep color, clear edges, and within the imaging depth of field range as the objects. A deep-learning-based super-resolution method was applied to enhance the image and improve the recognition of small-diameter droplets. The enhanced image was then binarized to extract the droplets within the imaging depth of field. To quantify the uncertainty introduced by the image processing procedure, a threshold sensitivity analysis was performed. The segmentation threshold was varied within ±5% of the nominal value, and the resulting variations in key spray parameters were evaluated. The changes in spray penetration length, mean diameter of droplets and cone angle were found to be within ±1 mm, ±0.003 mm and ±0.5°, respectively, and these values were taken as the image-processing uncertainty.

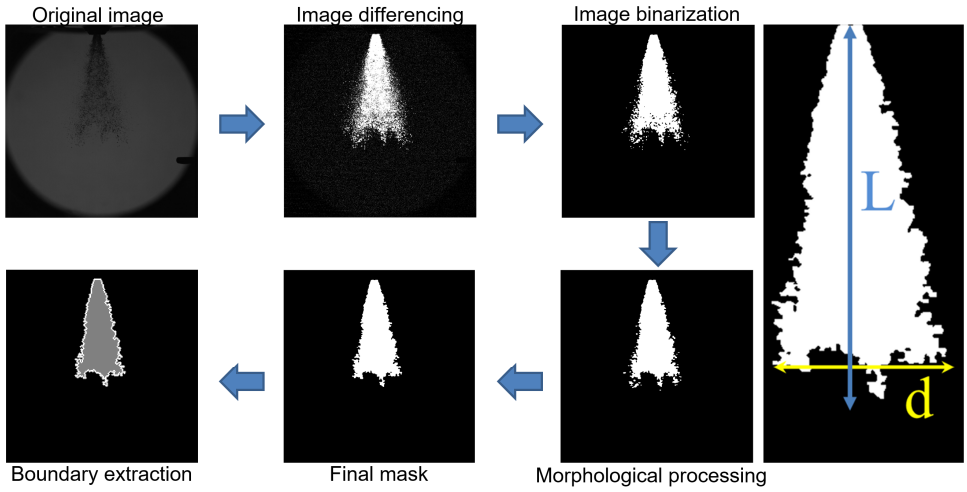
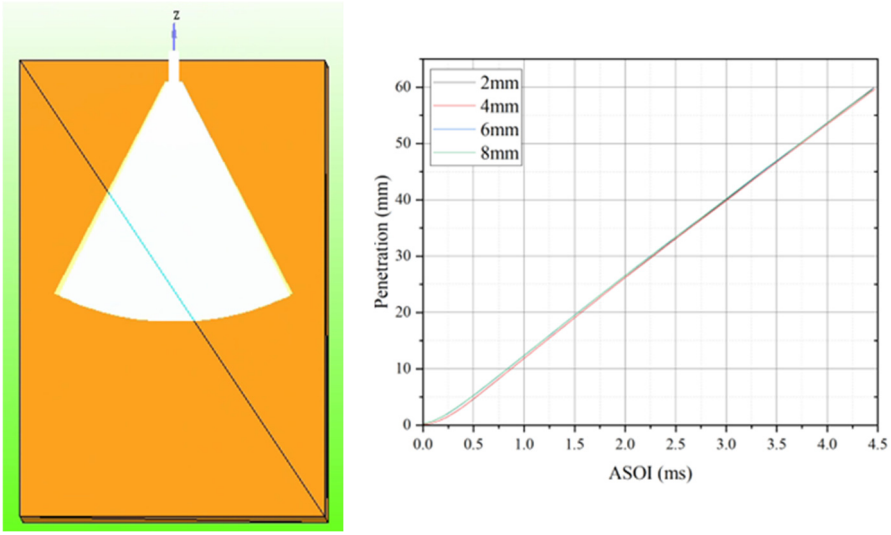


Figure 2. Spray image processing.

2.4. CFD Simulation Model Settings

The study used CONVERGE for three-dimensional transient spray simulations, and the geometric model is shown in Figure 3a. This software adopts the Euler–Lagrange framework, in which the continuous phase is described by solving the compressible Navier–Stokes equation, and the discrete phase droplets are solved by the particle tracking model. A structured mesh was used with adaptive local refinement. Mesh independence was verified for different mesh sizes, and the results are shown in Figure 3b. For grids of different sizes, we conducted grid independence verification. The results are shown in Figure 3b. When the grid size changed from 4 mm to 2 mm, the difference was only 0.16%. Therefore, the final selected base grid size was 4 mm, and the size near the nozzles was refined to 0.5 mm. The simulation models are listed in Table 3. Droplets were assumed to be spherical, and methanol was treated as a single-component fuel. Droplet evaporation was modeled as a convection-controlled process using the Frossling correlation [25], assuming uniform droplet temperature. Chemical reactions were neglected, and the simulations focused on non-reacting spray behavior. The ambient nitrogen was treated as an ideal gas. Spray–wall interaction was described using a wall-film model [26], assuming smooth walls and thin liquid films. Turbulence was modeled using the RNG k–ε model [27], which provides a Reynolds-averaged closure suitable for engine-relevant spray flows. Primary/secondary breakup was modeled using the KH–RT breakup model [28], which combines Kelvin–Helmholtz and Rayleigh–Taylor instabilities and has been extensively used and validated for high-pressure and vaporizing sprays in engine-relevant environments. Droplet collision

and coalescence were modeled using the No-Time-Counter (NTC) method [29], a standard collision algorithm for Lagrangian spray simulations.



(**a**) (**b**)

Figure 3. (**a**) Computational geometry model; (**b**) mesh-independence verification.

Table 3. Selection of the simulation model.

Parameter	Value
Breakup model	KH–RT model
Collision model	NTC model
Evaporation model	Frossling model
Spray–wall interaction	Wall Film model
Turbulence model	RNG k–ε model

3. Results and Discussion

3.1. The Influence of Temperature on Spray Morphology and Parameters

Figure 4 shows the temporal evolution of methanol spray morphology within the temperature range of 255–333 K under an ambient pressure of 0.1 MPa, an injection pressure of 0.4 MPa, and an injection pulse width of 5 ms. The experimental results indicate that methanol spray exhibits a typical two-stage breakup mechanism after injection. In the first stage, the liquid column undergoes primary breakup near the nozzle due to cavitation and near-field turbulence, forming relatively large droplet structures. This process is mainly governed by spray inertia and the fundamental physical properties of the fuel, such as viscosity and density. As the droplets travel downstream, the aerodynamic forces increase, and the relative velocity becomes sufficient to overcome droplet surface tension, triggering more intense secondary atomization and further droplet refinement. When the ambient temperature is within the range of 255–313 K, the spray initially shows axial extension. Lateral spreading to the left and right is not pronounced at the early stage but gradually increases as the spray develops, and the cone boundary tends to stabilize during the mid–late stages. Meanwhile, local disturbances and irregular structures appear in the downstream region (as circled in the figure). These features can be attributed to enhanced air entrainment and non-uniform fuel evaporation; turbulent fluctuations and transient phase change processes play important roles. As the ambient temperature rises from 255 K to 313 K, the spray contour area expands significantly and the degree of local expansion increases. This reflects that a higher ambient temperature will enhance the

spray kinetic energy and turbulence energy level, thereby strengthening the gas–liquid blending efficiency and entrainment capacity. When the temperature rises to 333 K, the spray structure undergoes significant changes: the leading edge of the spray beam shows an accelerating advancement trend, the evaporation of droplets on both sides is significantly intensified, and the overall spray gradually contracts towards the center line and forms a slender spindle-shaped liquid jet. The key to this phenomenon is that 333 K is close to the boiling point of methanol at 0.1 MPa. The increase in ambient temperature causes a rapid rise in saturated vapor pressure, significantly promoting the atomization process. At the same time, stronger interfacial disturbances between the spray and the surrounding gas enhance the vaporization rate of droplets at the spray boundary. In addition, the interaction between the fuel and the high-temperature wall caused some temperature unevenness, resulting in slight flash boiling and a significant change in the spray pattern.

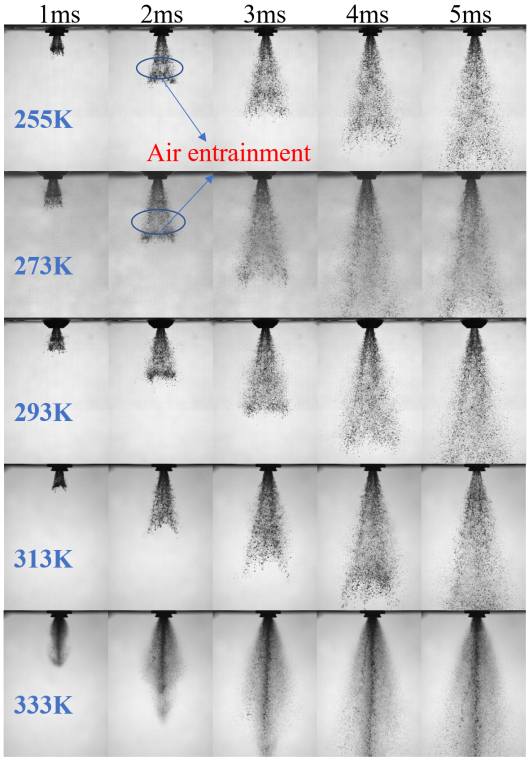


Figure 4. Temporal evolution of methanol sprays under different ambient temperatures.

Figure 5 illustrates the variations in spray penetration distance, cone angle, projected area, and particle size distribution within the ambient temperature range of 255–333 K. In the early stage of injection (before approximately 5 ms), the spray front advances rapidly, and the penetration distance increases almost linearly with time; the higher the ambient temperature, the steeper the slope of this linear increase. As time progresses, the propagation speed decreases, and the increment in penetration gradually diminishes. This is mainly due to the reduced ambient gas density at higher temperatures, which lowers the aerodynamic resistance encountered by the methanol jet; meanwhile, elevated temperatures enhance heat exchange between droplets and the surrounding gas, accelerating evaporation. The actual penetration distance is jointly determined by spray momentum and the entrainment capability of the surrounding air, both of which are affected by the latent heat of vaporization. Owing to methanol's high latent heat of vaporization, evaporation induces a pronounced local cooling zone around the spray. Under low-temperature conditions, this intensified cooling reduces the evaporation rate, allowing larger droplets to remain in the spray core region for a longer period, thus relatively shortening the penetration distance.

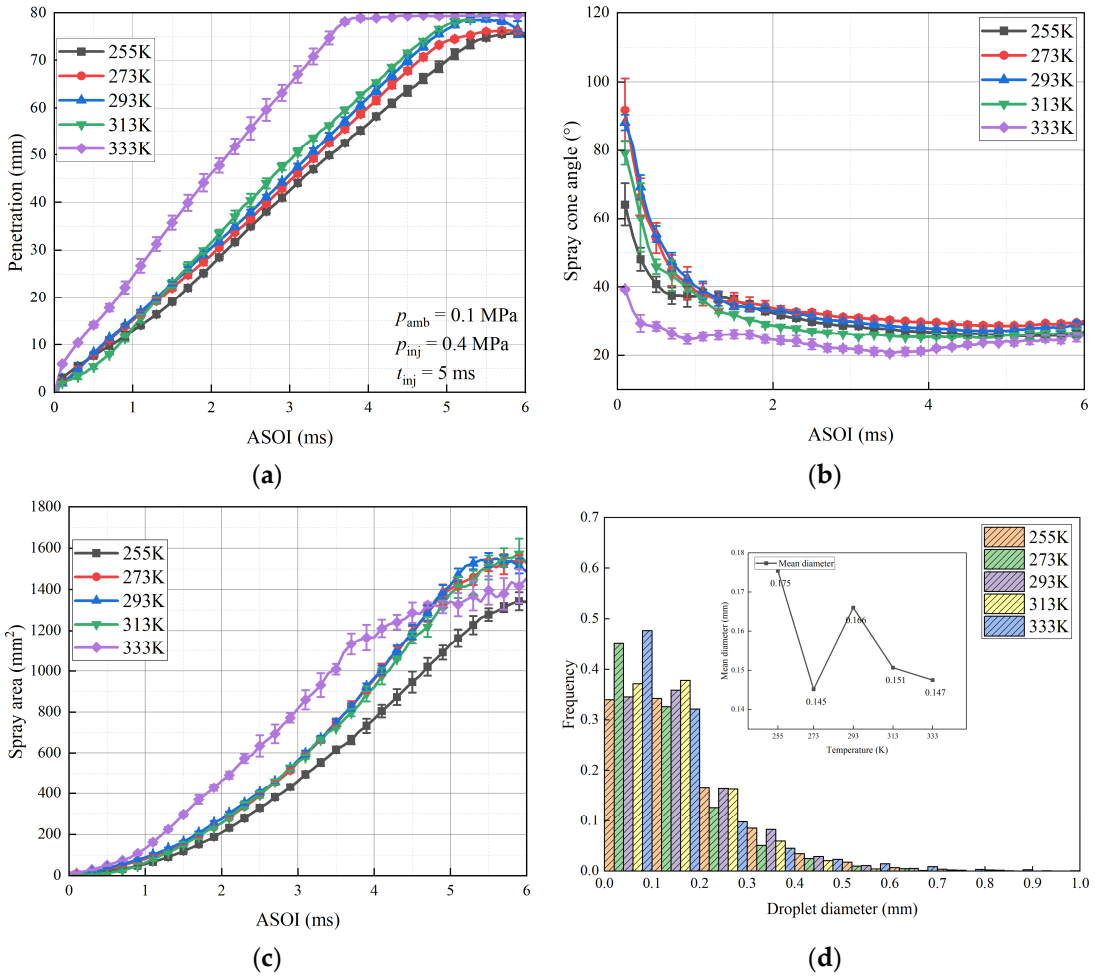


Figure 5. Effects of temperature on methanol spray characteristics: (**a**) spray penetration, (**b**) spray cone angle, (**c**) spray area, and (**d**) droplet size distribution.

The evolution of the spray cone angle at different temperatures is shown in Figure 5b. The initial cone angle is relatively large and then gradually decreases over time. This is mainly attributed to the interaction between the spray plumes and the contraction of the spray morphology caused by the strengthening of air entrainment. After approximately 3 ms, the cone angle enters a relatively stable range with a very small variation. As the ambient temperature changes from low to high, the average cone angle shows a trend of first increasing and then decreasing. The formation mechanism is rather complex: theoretically, an increase in temperature can enhance evaporation and gas-phase diffusion, thereby promoting the expansion of the spray boundary. However, at the same time, high temperatures reduce the environmental density, decrease the resistance near the spray outlet, and also drive the cone angle to increase. However, elevated temperatures accelerate the evaporation of small droplets at the spray periphery, causing the outer boundary of the spray to contract, thus reducing the cone angle. Below 273 K, the influence of ambient density is dominant, causing the cone angle to increase slightly with increasing temperature; when the temperature further rises to about 293 K and above, the enhanced evaporation effect becomes more prominent, thus significantly reducing the spray cone angle.

The spray area reflects the degree of spatial utilization of the surrounding environment by the spray. As shown in Figure 5c, the spray area remained nearly constant within the temperature range of 273–313 K, owing to the non-synchronous variation between the spray cone angle and penetration length. Due to the rapid movement of the spray outside

the viewing window range at 333 K, the spray area in the later stage was lower than that when the temperature was between 273 and 313 K.

Figure 5d illustrates the droplet size distributions under different ambient temperatures. As previously discussed, when the temperature increased from 255 K to 273 K, enhanced evaporation led to a reduction in the mean droplet diameter. With further temperature increase, the intensified evaporation caused the fine droplets near the spray periphery to vaporize more rapidly, reducing the proportion of small droplets and thereby increasing the average droplet size. When the temperature is further raised to approach the boiling point, the droplets evaporate vigorously, and there are a large number of small droplets on both sides of the spray Consequently, the average droplet diameter decreased again due to the high fraction of small droplets.

To validate the numerical model, two temperature conditions, 255 K and 313 K, were selected. Under an ambient pressure of 0.1 MPa, an injection pressure of 0.4 MPa, and an injection pulse width of 5 ms, the model was calibrated against the experimental spray penetration distance. The results are shown in Figure 6. The R^2 for both conditions reached 0.985, and the RMSE was less than 5% of the maximum penetration distance, indicating high model reliability. The resulting temperature and pressure distributions are presented in Figure 7.

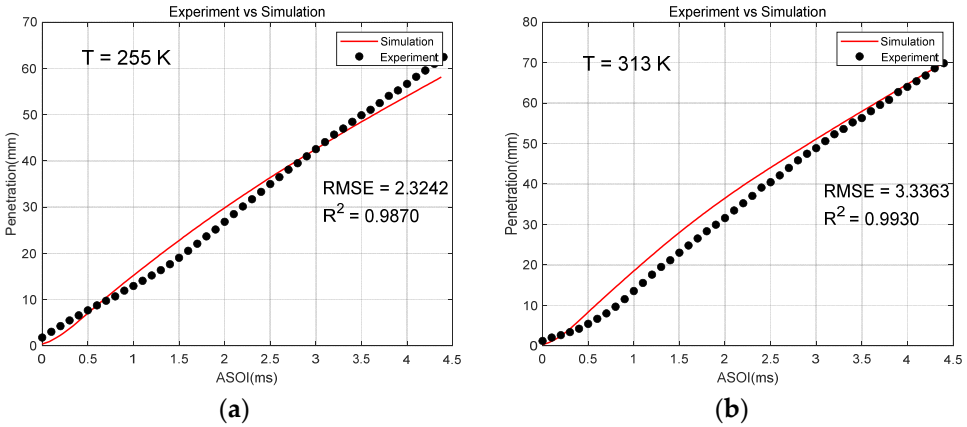


Figure 6. Comparison between simulation and experiment. (**a**) T = 255 K; (**b**) T = 313 K.

The simulated temperature field reveals significant differences in gas–liquid heat transfer during the spray process. Owing to the uniformity between the fuel and ambient temperatures, the heat-transfer gradient is small, resulting in limited thermal exchange that occurs mainly during droplet evaporation. At a temperature of 255 K, localized cooling nuclei were observed near the nozzle, with temperatures ranging from approximately 242 to 248 K. These nuclei had clear boundaries, indicating a narrow fuel evaporation zone and limited energy exchange with the environment. Over time, the low-temperature region remained optical intensity becomes darker concentrated and difficult to extend downstream. Meanwhile, no pronounced high-pressure wave appears at the nozzle exit; instead, a stable low-pressure zone forms within the spray core and gradually diffuses downstream. This low-pressure structure is caused by gas cooling and volume contraction due to evaporative heat absorption, resulting in weak entrainment. Because the spray momentum is low and gas compressibility is limited, the system remains in an overall pressure-deficit state, leading to sluggish diffusion. The local volume contraction induced by latent-heat absorption offsets gas compression, causing the static pressure throughout the spray region to remain lower than the ambient level.

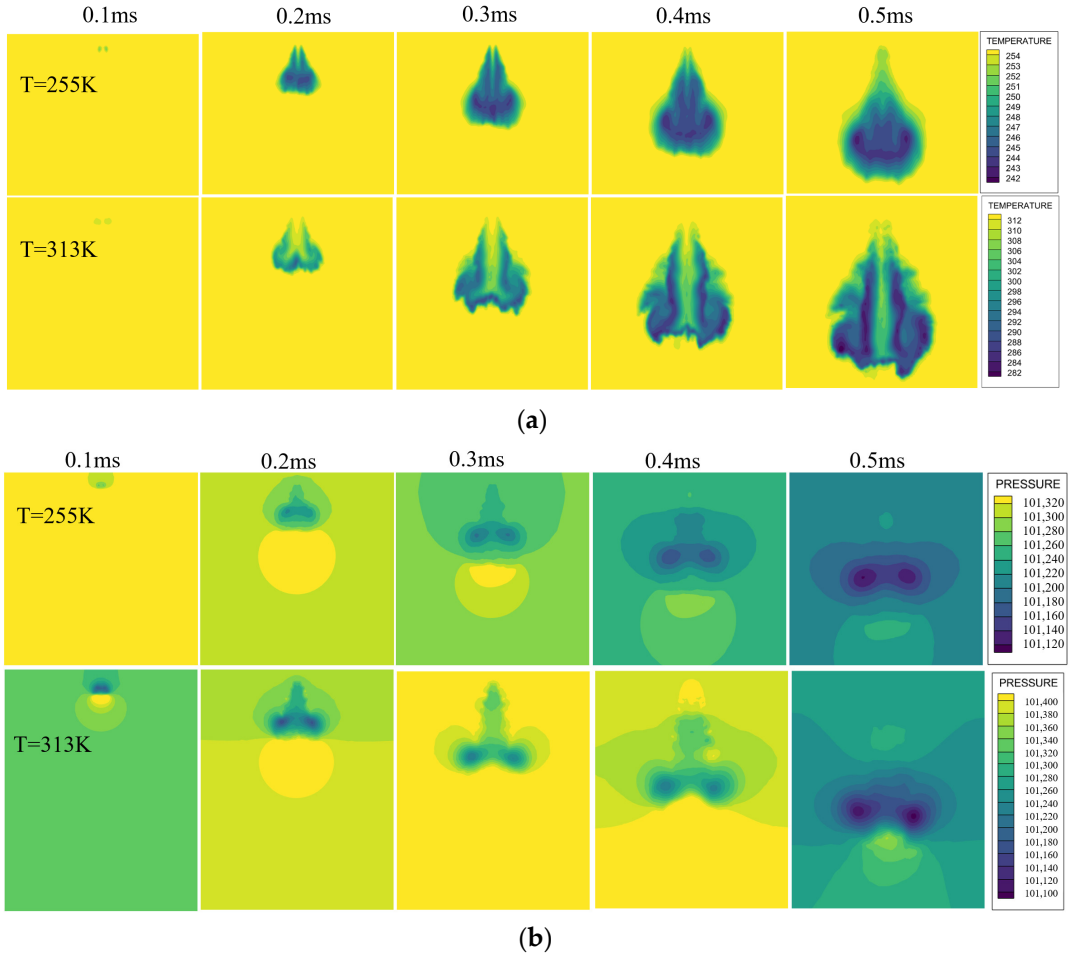


Figure 7. Temperature and pressure fields during spray development at 255 K and 313 K: (**a**) temperature field; (**b**) pressure field.

At 313 K, due to rapid fuel evaporation and intense heat exchange with the environment, a significant low-temperature plume structure appears within the spray. The cooling core temperature at this point is approximately 284–288 K. It can be observed that this region is highly consistent with the diffusion pattern at the spray leading edge, indicating that the temperature gradient induces density changes, leading to gas entrainment and recirculation. The blurred spray edge and refined droplets in the experimental images are consistent with this intense evaporation-cooling process. In the initial stage of injection, a significant high-pressure zone is observed near the nozzle, indicating that the momentum impact of the spray significantly compresses the air; subsequently, the high-pressure wave propagates outward and gradually attenuates, forming a symmetrical low-pressure dual-core structure in the spray region, inducing strong entrainment and recirculation vortices. This compression–expansion process, coupled with evaporative cooling, jointly drives plume diffusion and uniform mixture formation. The rapid expansion and edge dispersion of the spray in the experiment is a result of the continuous pressure evolution from momentum impact to compression wave propagation, and then to entrainment and backflow. Overall, at 313 K, the higher jet momentum and lower liquid viscosity give the spray higher kinetic energy, which can significantly compress the surrounding gas; thus, a short-term ultra-high-pressure zone is formed near the nozzle, which rapidly attenuates during the subsequent expansion. The higher temperature also reduces the gas density and enhances its compressibility, making the pressure fluctuation propagation more significant. In contrast, under low-temperature conditions, the spray is dominated by evaporative en-

dothermic behavior, exhibiting continuous low-pressure diffusion. Under high-temperature conditions, however, the spray is dominated by momentum-driven impact, showing pressure fluctuations that first rise and then fall, accompanied by strong entrainment—this being the fundamental reason for the rapid plume expansion observed experimentally.

3.2. The Influence of Environmental Pressure on Spray Morphology and Parameters

Figure 8 shows the development of methanol spray over time under different ambient pressures. At 255 K, as ambient pressure increases, the methanol spray tip becomes smoother, as can be observed in the images. This phenomenon indicates that increased environmental pressure enhances the interaction between the spray and the surrounding air, exacerbating air entrainment and droplet breakup, resulting in a denser spray structure and a smoother spray tip. At 333 K, the elevated temperature greatly enhances spray atomization. At 0.05 MPa in particular, where the methanol temperature exceeds its boiling point, pronounced flash boiling occurs. Compared to 0.1 MPa, the spray moves at a faster speed and evaporates more violently, making it impossible to distinguish individual droplets in the image. The spray expands rapidly on both sides, significantly increasing the overall coverage area. At 0.2 MPa, the spray pattern did not change significantly because the temperature of methanol was much lower than its boiling point.

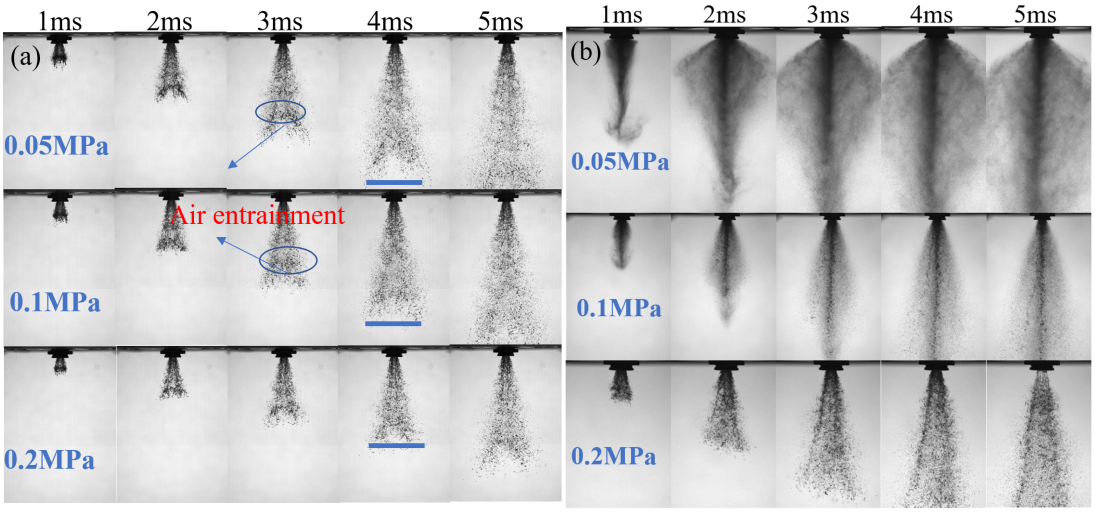


Figure 8. Temporal evolution of methanol sprays under different ambient pressures: (**a**) 255 K, (**b**) 333 K.

Figure 9 shows the spray penetration distance, spray cone angle, spray area, and particle size distribution of high-pressure methanol spray under different ambient pressures. The results show that the growth of the spray penetration distance presents a linear trend, and the length gradually decreases as the ambient pressure increases, suggesting that the spray velocity remains relatively constant. According to Bernoulli's equation, the theoretical velocity at the nozzle exit is influenced by fuel density and the pressure difference between ambient pressure and injection pressure. An increase in ambient pressure will reduce the pressure difference, thus decreasing the initial velocity and momentum of the droplets. Based on empirical correlations [30,31], the penetration distance of methanol sprays can be expressed as

$$L = K_v \frac{\sqrt{2\Delta P}}{\rho_f} t \quad (1)$$

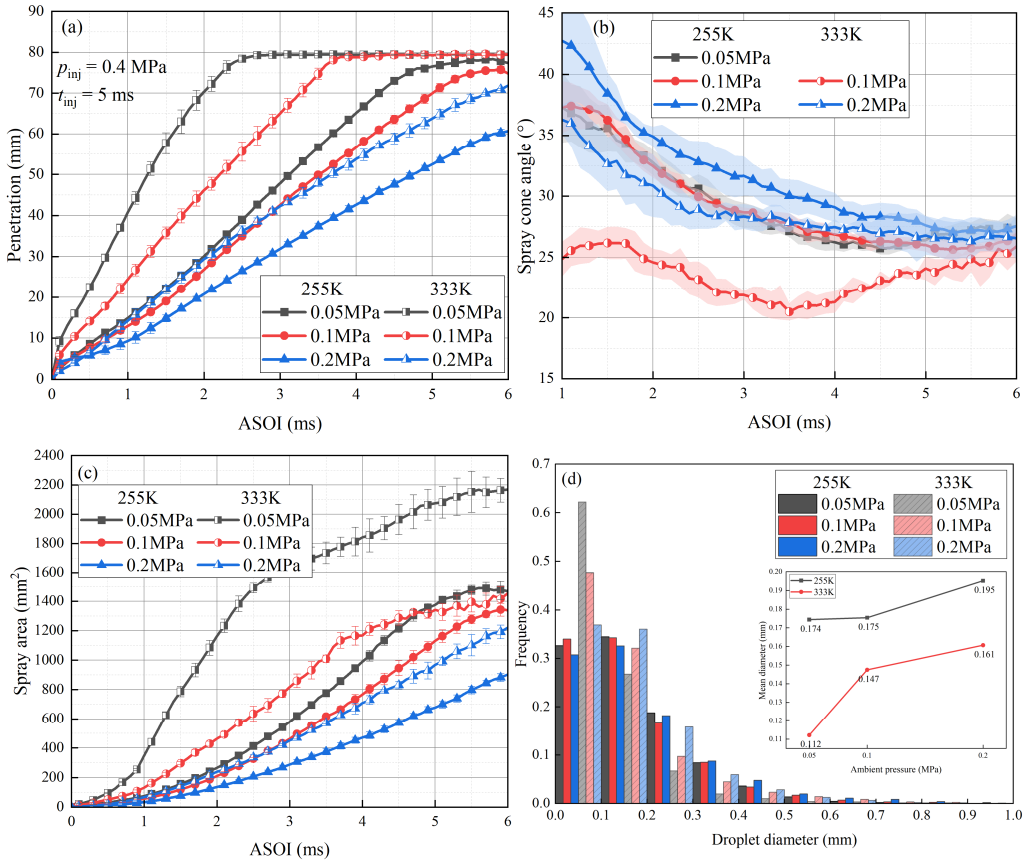


Figure 9. Effects of ambient pressures on methanol spray characteristics: (**a**) spray penetration, (**b**) spray cone angle, (**c**) spray area, and (**d**) droplet size distribution.

Here, K_v is a model constant, ρ_f represents the density of methanol, ΔP denotes the pressure difference, and t is the time. As the ambient pressure increases, the value of ΔP decreases, leading to a corresponding reduction in spray penetration length.

Furthermore, another reason for this reduction is that the increased ambient pressure increases the drag on fuel droplets, as expressed in Equation (2) [32]:

$$D = C_d \frac{\rho V^2 A}{2} \tag{2}$$

Here, D represents the drag force, C_d is the experimentally determined drag coefficient, ρ denotes the ambient gas density, A is the surface area associated with frictional resistance, and V is the droplet velocity. A higher drag force results in greater axial momentum loss, thereby reducing the spray penetration length.

An increase in ambient pressure leads to a shorter methanol spray penetration length, while the spray cone angle exhibits the opposite trend—an observation consistent with that reported for gasoline and diesel sprays [33–35]. As ambient pressure rises, the spray cone angle increases noticeably because the interaction between the surrounding air and the spray is strengthened due to the higher gas density [34,35]. This enhanced aerodynamic coupling promotes droplet dispersion, particularly for fine droplets near the spray periphery. In addition, the reduction in spray velocity under high ambient pressure diminishes the effect of air entrainment. This phenomenon also agrees well with the empirical correlation given by Equation (3) [10]:

$$\theta = C\left(\frac{D_n^2 \rho \Delta P}{\mu}\right)^{0.25} \tag{3}$$

Here, μ and ρ represent the dynamic viscosity and density of the ambient gas, respectively; D_n denotes the nozzle diameter; and C is a model constant. When the ambient pressure increases, a smaller ΔP leads to a narrower cone angle. However, the higher gas density ρ enhances the aerodynamic resistance within the constant-volume chamber, which in turn promotes lateral dispersion and broadens the spray cone angle.

Under different ambient pressures, the spray area increases approximately proportionally with time, but its magnitude decreases markedly at higher ambient pressures. Both spray penetration length and spray cone angle influence the overall spray area: a longer penetration length and a wider cone angle contribute to a larger spray coverage. Nevertheless, as ambient pressure increases, the penetration length decreases sharply. Since spray penetration dominates the determination of the liquid-phase spray area, elevated ambient pressure ultimately results in a reduction in spray area. The mean droplet diameter also increases with ambient pressure, indicating less effective atomization under denser gas conditions. Additionally, the results show that after flash boiling occurs, a large number of fine droplets are generated, signifying that this condition significantly promotes methanol evaporation and enhances phase transition dynamics within the spray plume.

Figure 10 illustrates the evolution of the temperature and pressure fields of methanol sprays at an ambient temperature of 255 K and an injection pressure of 0.4 MPa, under ambient pressures of 0.05 MPa, 0.1 MPa, and 0.2 MPa. At an ambient pressure of 0.05 MPa, the cooling core expanded rapidly within 0.3–0.5 ms, reaching a minimum temperature of approximately 232–236 K, and nearly covering the entire spray plume region. This indicates that under low-pressure conditions, droplet evaporation is extremely intense, the vaporization rate increases significantly, and the absorption of large amounts of latent heat of vaporization leads to strong local gas cooling. The experimentally observed blurred spray boundaries and hollow plume structures originate from this intense thermo-fluid coupling effect caused by high-rate evaporation. When the ambient pressure was increased to 0.1 MPa, the cooling core became more concentrated and symmetric, with a temperature difference of about 10–15 K across the spray region. At this stage, droplet evaporation and gas–air convective heat transfer approach equilibrium, resulting in high evaporation efficiency and stable atomization. This corresponds to the experimental condition with the most uniform plume structure and the most appropriate cone angle. At an ambient pressure of 0.2 MPa, the volume of the cooling core decreases significantly, mainly concentrated below the nozzle, with a minimum temperature of only 242–245 K. Increased ambient pressure inhibits droplet evaporation and vapor diffusion, thus the spray zone is dominated by the liquid phase.

The pressure field further reveals the dynamic differences in spray behavior under different back-pressure conditions. In a low-pressure environment, a short-lived high-pressure cluster first appears at the nozzle exit, then rapidly decays, forming a large-scale negative-pressure zone within the main spray body. Due to the low ambient gas density and low flow resistance, the spray induces strong entrainment, and the diffusion of negative pressure enhances air entrainment. This phenomenon is highly consistent with the plume-boundary instability and the "hollow spray" features observed in the experiment. Under 0.1 MPa conditions, a slightly high-pressure core initially exists in the nozzle neighborhood, which gradually transforms into a symmetrical low-pressure dual-core structure with a relatively small degree of negative pressure. At this point, momentum diffusion and entrainment processes are in balance, and the gas forms a stable reflux, which helps to break up droplets and homogenize the mixture.

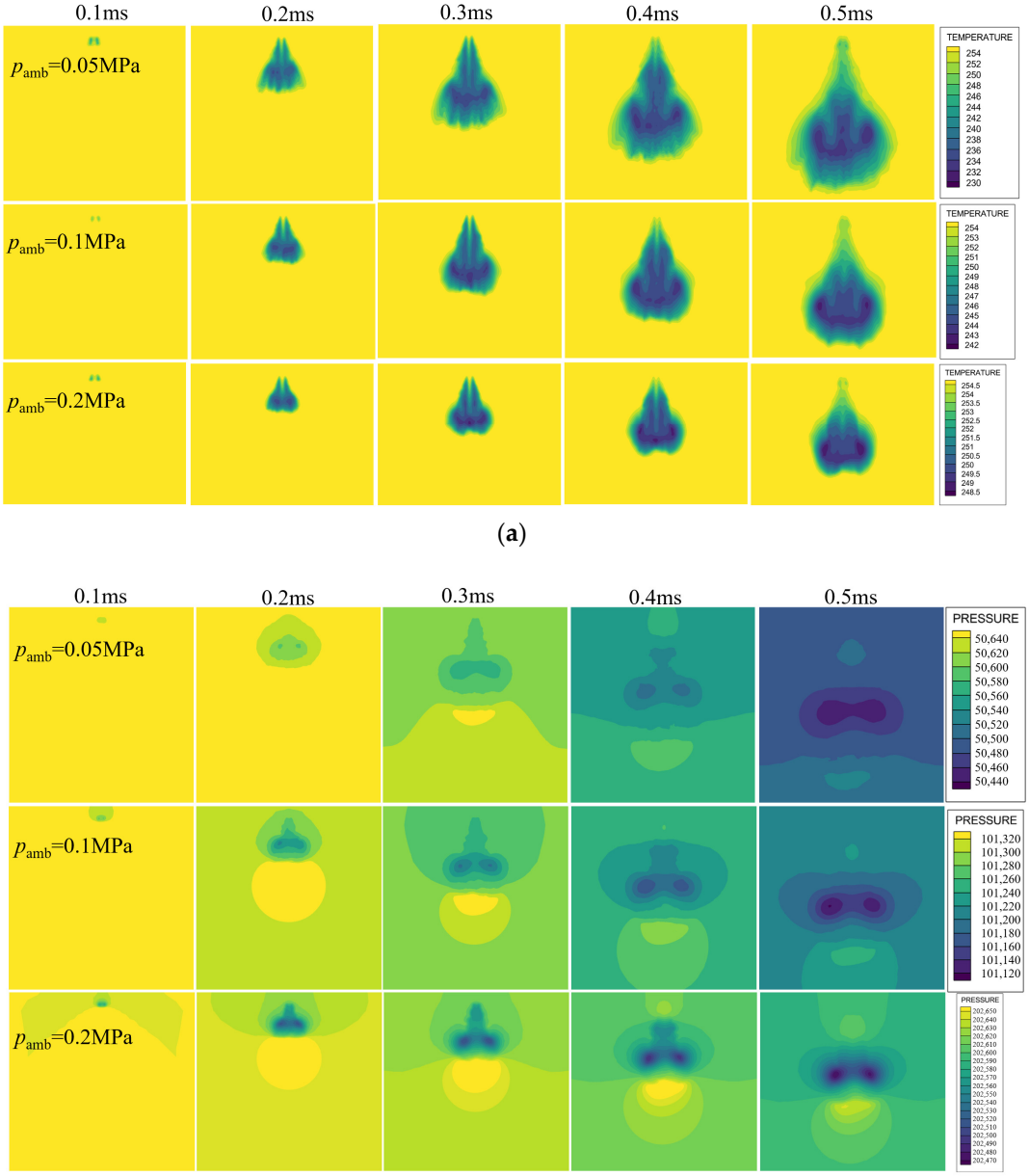


Figure 10. Temperature and pressure fields during spray development under different ambient pressures. (**a**) Temperature field; (**b**) pressure field.

Under the 0.2 MPa condition, the pressure drop at the spray leading edge is substantially reduced, and the overall pressure field tends to stabilize. The higher gas density and stronger drag limit momentum diffusion, suppressing both entrainment and recirculation. As the ambient back pressure increases, the spray cone angle shows an increasing trend in the visualization images, whereas the low-temperature region in the temperature field exhibits contraction. This contrast arises from the different dominant roles of macroscopic flow structures and microscopic heat-transfer mechanisms. Higher back pressure increases gas density and turbulent shear, enhancing droplet breakup and strengthening radial entrainment, thereby increasing the geometric spray cone angle. At the same time, however, the high-pressure environment inhibits evaporation and vapor diffusion, causing latent-heat absorption to remain concentrated near the spray center, reducing the cooling-core size and the extent of the low-temperature region.

Therefore, under high environmental pressure, although the spray exhibits an increased cone angle geometrically, its thermodynamic distribution shows a more concentrated region. This is a typical manifestation of the coupling effect of flow and heat transfer in methanol spray under different environmental pressures. This contrast between geometric diffusion and thermal-core shrinkage is a typical manifestation of the coupled flow–heat transfer behavior of methanol sprays under varying ambient pressures.

3.3. The Influence of Spray Strategies on Spray Morphology and Parameters

Figure 11 presents methanol spray images at ambient temperatures of 255 K and 333 K, an ambient pressure of 0.1 MPa, and different injection strategies. At 255 K, when the injection pressure increases from 0.4 MPa to 0.6 MPa, the spray diffusion rate increases significantly, and the penetration length is noticeably extended. Under higher injection pressure, the liquid column core exhibits a higher particle concentration, while the spray periphery shows more complete atomization. In contrast, variations in injection pulse width have little influence on spray morphology during the initial 2 ms of development. At 333 K, increasing injection pressure clearly leads to a weakened flash-boiling effect in the methanol spray. The overall optical intensity of the spray becomes darker, and large droplets are observed to expand outward from the central region. Similarly, the influence of injection pulse width on spray morphology remains minimal during the early stage (before 2 ms). These observations indicate that injection pressure predominantly governs spray momentum and atomization intensity, whereas pulse width primarily affects fuel mass delivery and thus has a delayed impact on spray structure. At higher temperatures, the combined effects of increased vapor pressure and enhanced evaporation weaken flash boiling, leading to more uniform droplet distribution and improved spray stability.

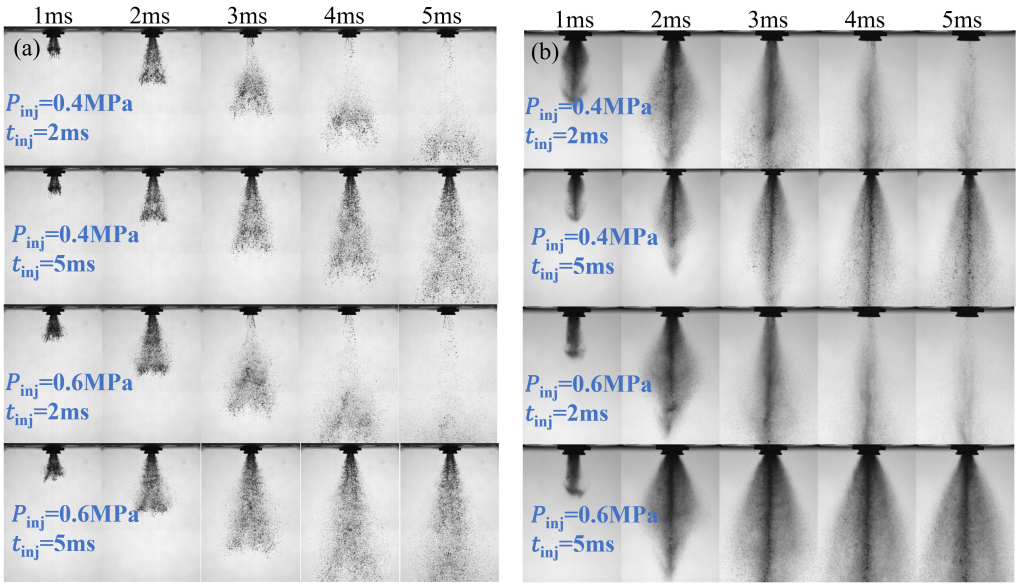


Figure 11. Temporal evolution of methanol sprays under different injection strategies: (**a**) 255 K, (**b**) 333 K.

Figure 12 shows the variations in spray penetration length, spray cone angle, spray area, and droplet size distribution of methanol sprays at 255 K under different injection strategies. As observed, although the injection pulse width increases from 2 ms to 5 ms, the penetration length and spray area of both cases remain nearly identical within the first 3 ms. Beyond this time, the 2 ms group ceases fuel injection, and as the previously injected fuel gradually evaporates, both the penetration length and spray area decrease compared with those of the 5 ms group. This trend agrees well with the phenomena observed in the spray images. According to Equation (3), increasing the injection pressure enhances the pressure

difference ΔP, thereby increasing both penetration length and spray area. The spray cone angle also widens with increasing injection pressure but shows no clear dependence on pulse width. At higher injection pressure, droplets possess greater initial momentum, enabling them to spread more readily in the radial direction. For the droplet size, sprays with shorter injection pulse widths exhibit smaller average diameters. This is because the shorter pulse ends earlier, delivering a smaller fuel quantity, resulting in fewer droplet collisions and allowing more complete atomization. As the spray front approaches the optical field boundary, the mean droplet size reaches its minimum. An increase in injection pressure generally leads to smaller droplet sizes; however, at a pulse width of 5 ms, no significant reduction in average diameter is observed. Instead, the droplet size distribution becomes more uniform, which may be attributed to intensified interaction between droplets and the surrounding gas, promoting evaporation of fine droplets and homogenization of the overall distribution.

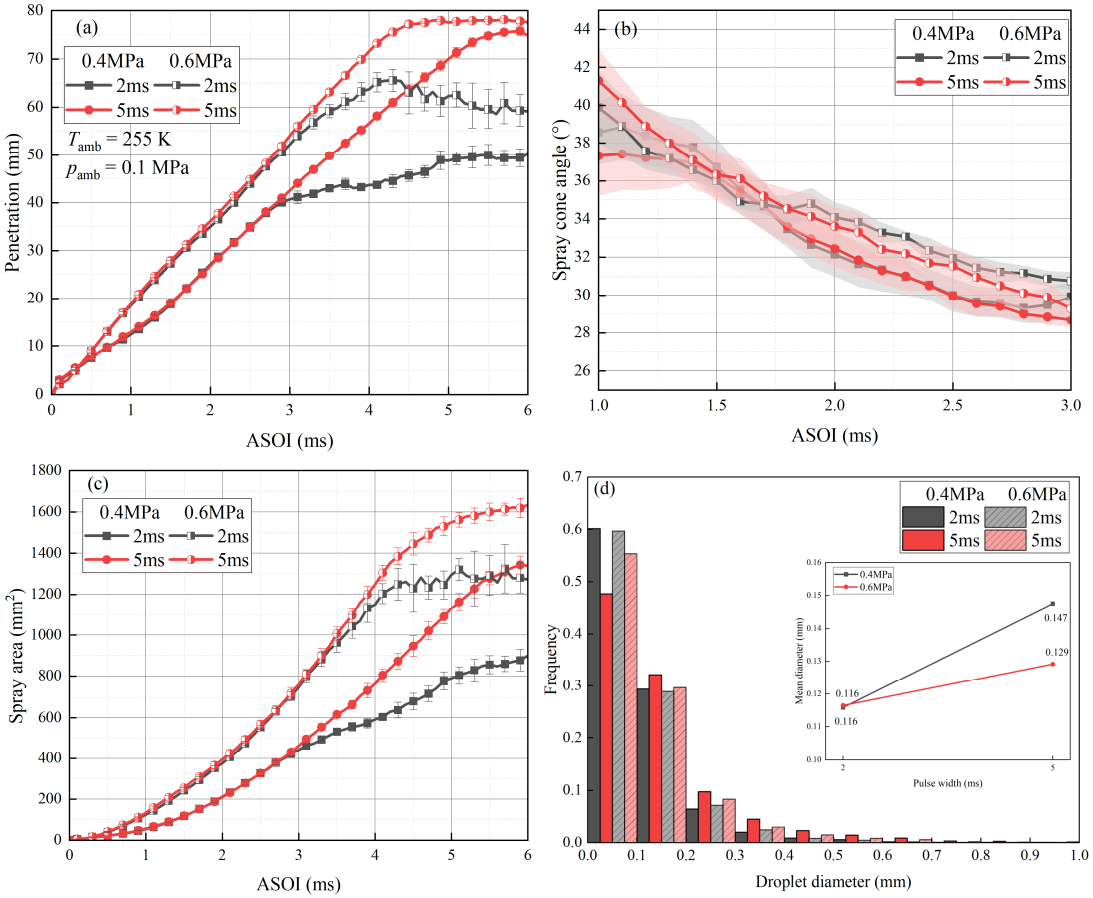


Figure 12. Effects of injection strategies on methanol spray characteristics at 255 K: (**a**) spray penetration, (**b**) spray cone angle, (**c**) spray area, and (**d**) droplet size distribution.

Since the influence of injection pulse width on spray morphology is relatively minor, this section focuses on analyzing the spray characteristics under different injection pressures, using an ambient temperature of 255 K as the comparison condition, as shown in Figure 13. At an injection pressure of 0.4 MPa, the cooling core forms slowly and remains relatively concentrated, with a minimum temperature of approximately 242 K, primarily confined to the region directly beneath the nozzle. The cooling zone exhibits a well-defined and symmetric shape, indicating that the evaporation process is strongly constrained, with latent heat absorption localized within the liquid column core and limited vapor-phase expansion. This observation aligns well with the experimental finding of a clear liquid column and weak atomization under low-pressure conditions. When the injection pressure

is increased to 0.6 MPa, the cooling core expands rapidly—within approximately 0.3 ms after injection—and extends toward the spray front. The minimum temperature further decreases to 241 K, and the area of the cooling region increases substantially, indicating a more vigorous evaporation process. The higher injection momentum enhances gas–liquid interfacial disturbances, leading to a significant increase in the droplet surface area, thereby intensifying the evaporative cooling effect. The temperature field results demonstrate that as the injection pressure rises, both droplet kinetic energy and turbulent intensity increase simultaneously. The entrainment effect is markedly strengthened, and both heat transfer and evaporation rate are accelerated. Consequently, the spray morphology transitions from a concentrated liquid column to a dispersed plume, reflecting a shift from momentum-limited to turbulence-enhanced atomization behavior.

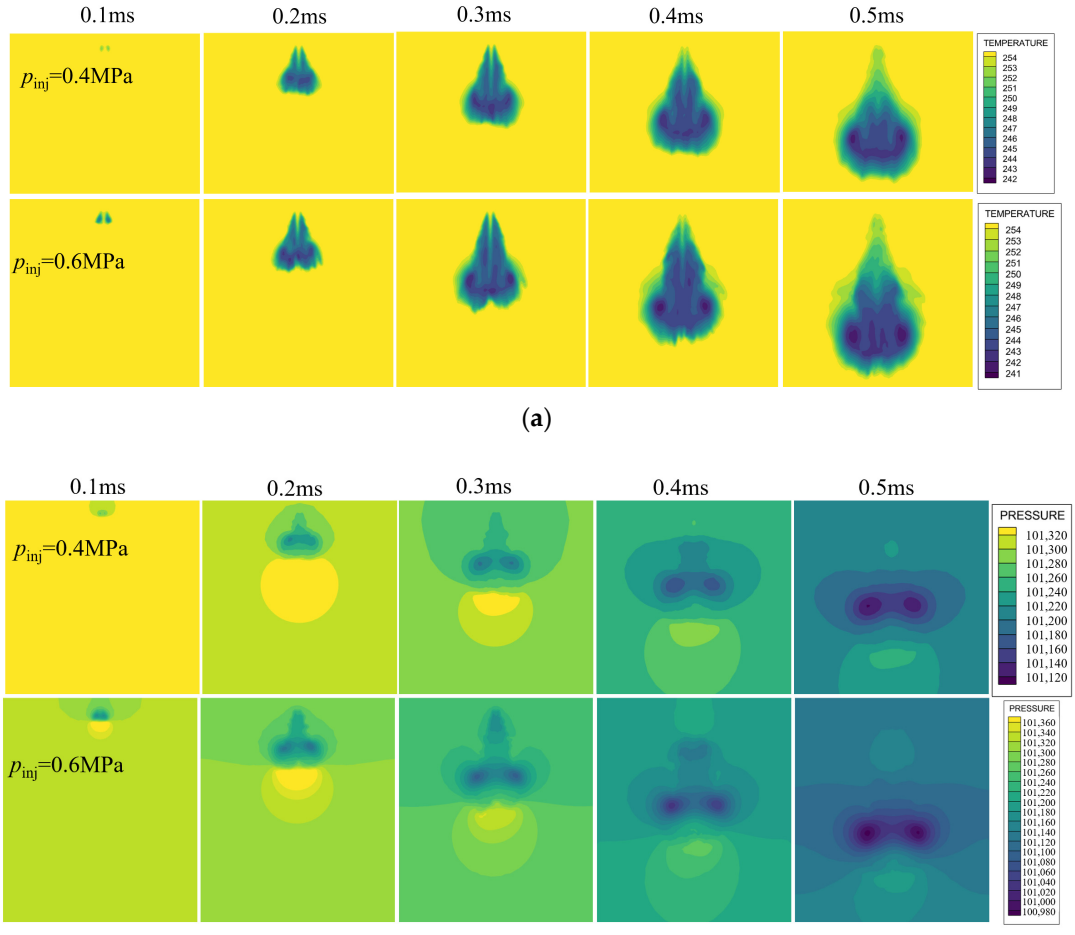


Figure 13. Temperature and pressure fields during spray development under different injection pressures. (**a**) Temperature field; (**b**) pressure field.

The pressure field distribution further reveals the differences in aerodynamic response mechanisms under varying injection pressures. At an injection pressure of 0.4 MPa, a small high-pressure core (approximately 101,300 Pa) forms near the nozzle exit, which rapidly decays and evolves into a symmetric low-pressure region (around 101,200 Pa). The extent of the low-pressure zone is limited, and the entrainment effect is weak, indicating that the spray momentum is insufficient to significantly compress the surrounding gas. As a result, the spray expansion is primarily governed by viscous diffusion, leading to a narrow plume and short penetration length, consistent with the experimental observations. When the injection pressure is increased to 0.6 MPa, a stronger high-pressure cluster (approximately 101,340 Pa) forms near the nozzle exit and subsequently propagates downstream along

the spray axis, rapidly transitioning into a broader low-pressure region (approximately 101,100 Pa). The high-momentum jet triggers a pronounced compression–expansion wave, which intensifies gas motion and significantly enlarges both the entrainment and recirculation zones. The expanded negative-pressure region promotes enhanced air entrainment and fuel–air mixing, corresponding to the experimentally observed accelerated atomization and increased plume diffusivity. In summary, as the injection pressure increases, both the strength of the compression wave at the nozzle exit and the magnitude of the subsequent low-pressure recirculation are markedly amplified. The spray transitions from a low-speed, viscous diffusion regime to a high-momentum, impact–entrainment-dominated regime. This transition not only strengthens the aerodynamic interaction between the spray and the surrounding gas but also significantly enhances the evaporation and mixing characteristics, thereby improving overall atomization performance.

Figure 14 presents the results of spray penetration length, spray cone angle, spray area, and droplet size distribution for methanol sprays at 333 K under different injection strategies. At elevated temperature, the spray motion velocity increases noticeably, and the delay in spray development caused by higher injection pressure becomes more pronounced during the initial stage. In particular, due to the occurrence of mild flash boiling, the spray tip velocity is already high, so further increasing injection pressure produces only a limited effect on penetration length. The variation trends of spray cone angle and spray area are generally consistent with those observed at 255 K, while the average droplet diameter shows a significant reduction compared with the lower-temperature condition. This reduction indicates enhanced atomization and evaporation under high-temperature conditions, as elevated ambient temperature weakens liquid cohesion, promotes droplet breakup, and accelerates phase change—ultimately improving fuel–air mixing efficiency.

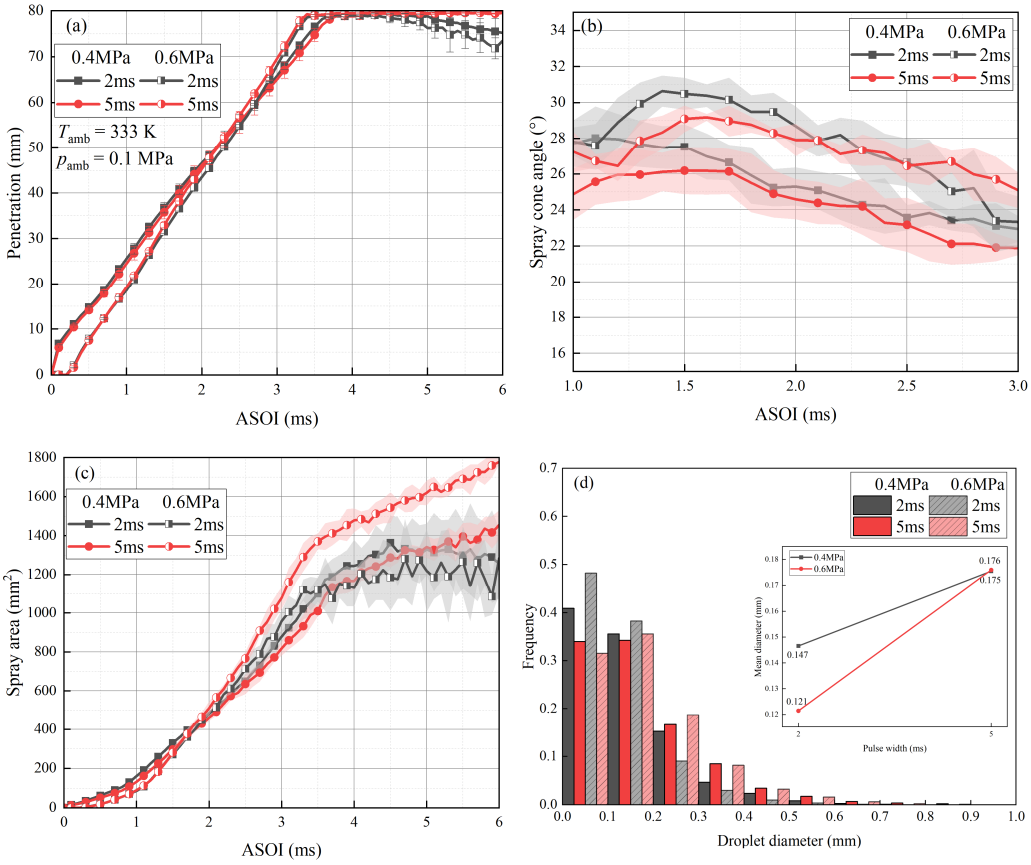


Figure 14. Effects of injection strategies on methanol spray characteristics at 333 K: (**a**) spray penetration, (**b**) spray cone angle, (**c**) spray area, and (**d**) droplet size distribution.

3.4. Improvement of Engine Cold Start

The experimental spray images and simulated temperature and pressure field results reveal that the main difficulty faced by the methanol spray in PFI engines during the cold start phase at low temperatures stems from the persistent presence of the cooling core, which inhibits fuel evaporation. For example, at an ambient temperature of 255 K, the experimental images show a uniform grayscale distribution at the outer edge of the spray plume but low overall brightness, indicating that evaporation is hindered in the initial diffusion stage, and the droplets are difficult to fully vaporize after atomization. As time progresses, the overall spray morphology remains a cold columnar structure, indicating insufficient core fragmentation and a limited evaporation rate.

Correspondingly, the temperature-field simulation shows that under the same operating conditions, the temperature in the spray core region drops rapidly, with a minimum of approximately 242–245 K. The cooling core forms a narrow, elongated column along the spray axis, characterized by dense isotherms and sharply defined boundaries. The temperature at the outer spray edge remains above 250 K, consistent with the experimentally observed high brightness at the plume periphery and the incomplete evaporation of droplets. The presence of a concentrated cold core significantly reduces the area of fuel gasification, weakens air entrainment and mixing, and further leads to uneven distribution of the mixed gas field, which has an adverse effect on subsequent ignition.

When the ambient temperature increases to 313 K, the experimental images show that the spray rapidly transitions into a plume-like structure, accompanied by significantly smaller droplet sizes and more complete atomization. The grayscale distribution at the plume edge becomes diffuse, indicating enhanced evaporation. The corresponding simulation results show that the cooling core changes from a concentrated columnar structure to a diffuse plume-like region, the low-temperature region expands significantly, and the boundary becomes blurred, reflecting enhanced air entrainment and mixing.

The consistency between experimental and simulation results indicates that under cold-start conditions, delayed fuel evaporation and cooling-core formation are the direct causes of hindered vaporization. As ambient temperature rises, weakening of the cooling core, enhanced mixing, and earlier formation of combustible nuclei become the key physical factors enabling improved cold-start performance.

To address the challenges of a persistent cooling core, limited evaporation, and uneven mixing at low temperatures, the following optimization strategies can be proposed:

1. Intake air or injector heating to weaken the cooling core and alleviate evaporation delay;
2. High-pressure, short-duration pre-injection to disrupt the liquid core and form an initial combustible kernel;
3. Optimized spark plug placement in the high-temperature, combustible periphery to avoid the cooling core region.

4. Conclusions

This study systematically investigated the effects of ambient temperature, pressure, and injection strategy on the characteristics of low-pressure methanol sprays by combining constant-volume combustion chamber experiments with CFD numerical simulations. The evolution mechanisms of methanol sprays under both low- and high-temperature conditions were elucidated, providing practical insights into engine cold-start optimization and combustion control. The main conclusions are as follows:

1. Spray atomization and evaporation are strongly influenced by ambient temperature. As the temperature increases from 255 K to 333 K, the spray penetration length increases by approximately 70%, accompanied by significant enhancement in evaporation. Under low-temperature conditions, a persistent cooling core forms with a

dense liquid core and long penetration distance, which inhibits vaporization and delays mixture formation—this constitutes the fundamental thermodynamic cause of cold-start difficulty. At higher temperatures, localized flash boiling occurs, markedly accelerating atomization and evaporation; the cooling core rapidly dissipates, resulting in a more uniform combustible mixture. However, when the temperature exceeds 313 K, excessive penetration increases the risk of wall impingement and pre-ignition.

2. Ambient pressure governs spray dynamics through the gas–liquid momentum ratio. Ambient pressure significantly affects the macroscopic behavior of low-pressure methanol sprays. Increasing ambient pressure reduces both spray velocity and penetration length due to the smaller pressure differential between the injection and ambient pressures. Meanwhile, the higher gas density enhances interaction between the spray and surrounding air, leading to a wider spray cone angle. In addition, droplet size increases with rising ambient pressure, reflecting reduced atomization efficiency.
3. Adjusting injection strategy effectively improves atomization performance. Increasing the injection pressure from 0.4 MPa to 0.6 MPa shortens the liquid column core, reduces the average droplet diameter by approximately 15%, and enhances spray uniformity. Appropriately shortening the injection pulse width (from 5 ms to 2 ms) decreases droplet collision probability and mitigates wall impingement.
4. Optimization strategies for low-temperature cold-start. Both experimental and simulation results confirm that restricted evaporation and the persistent cooling core are the primary challenges to cold-start performance. To address these issues, the following recommendations are proposed:
    (1) Intake air or injector heating to weaken the cooling core and alleviate evaporation delay;
    (2) High-pressure, short-duration pre-injection to disrupt the liquid core and form an initial combustible kernel;
    (3) Optimized spark plug placement in the high-temperature, combustible periphery to avoid the cooling core region.

Overall, this study quantitatively characterized the spatiotemporal evolution of the cooling core in methanol sprays through a combined experimental–numerical approach. The results provide directly applicable experimental and simulation parameters for spray model calibration, injector design, and intake thermal management in PFI methanol engines, as well as strategic guidance for improving cold-start performance in methanol-fueled engines.

5. Limitations and Future Work

The present study investigates methanol spray behavior under controlled, non-reacting conditions in a constant-volume combustion chamber using combined experimental and numerical approaches. This framework enables systematic isolation of the effects of ambient temperature, ambient pressure, and injection parameters on spray atomization and evaporation; however, several limitations should be noted.

First, chemical reactions were not considered in the CFD simulations, and the analysis was restricted to non-reacting spray processes. As a result, the coupling between spray evolution, ignition, and combustion under real engine conditions was not addressed. Second, methanol was modeled as a single-component fuel, and simplified sub-models were employed for droplet breakup, evaporation, turbulence, and spray–wall interaction. Although these models are widely adopted and validated in prior studies, they may not fully capture microscale phenomena, particularly under extreme low-temperature or high-pressure conditions. Third, the investigated operating conditions were limited to a specific range of ambient states and injection strategies associated with the present experimental setup; therefore, the conclusions should be interpreted within this defined parameter space.

Future work will extend the present framework to reacting spray and combustion conditions to clarify the coupling between spray dynamics and ignition behavior. Broader injection pressures, alternative nozzle geometries, and transient boundary conditions will also be considered to enhance engine relevance. In addition, optimization-oriented studies incorporating application-specific performance metrics will be conducted to identify optimal spray and injection strategies for improved mixture formation and cold-start performance.

Author Contributions: Conceptualization, D.W. and W.Z.; methodology, W.Z.; validation, W.Z.; formal analysis, C.Z.; investigation, W.Z.; resources, Z.L.; data curation, X.Z.; writing—original draft preparation, W.Z. and K.S.; writing—review and editing, Y.Q. and Z.W.; visualization, W.Z.; supervision, D.W. All authors have read and agreed to the published version of the manuscript.

Funding: This research was funded by National Key Research and Development Program of China (2024YFB2505400) and Taishan Industrial Experts Program (Guobo2024-015ZX).

Data Availability Statement: The data presented in this study are available on request from the corresponding author. They are restricted to experimental results.

Conflicts of Interest: Authors Decheng Wang, Zhijie Li, Changhui Zhai, Xiaoxiao Zeng, and Kui Shi were employed by the Weichai Power Co., Ltd. The remaining authors declare that the research was conducted in the absence of any commercial or financial relationships that could be construed as a potential conflict of interest.

References

1. Yan, Y.; Liu, Z.; Liu, J. Computational analysis of ammonia-hydrogen blends in homogeneous charge compression ignition engine operation. *Process Saf. Environ. Prot.* **2024**, *190*, 1263–1272. [CrossRef]
2. Wang, X.; Bu, H.; Chen, H.; Liu, J.; Chen, Z.; Gao, J. Numerical investigation of diesel spray combustion characteristics in the ammonia/air atmosphere. *J. Energy Inst.* **2024**, *116*, 101718. [CrossRef]
3. Eurostat. *Complete Energy Balances*; Eurostat: Luxembourg, 2025. [CrossRef]
4. Jiang, M.; Sun, W.; Guo, L.; Zhang, H.; Jia, Z.; Qin, Z.; Zhu, G.; Yu, C.; Zhang, J. Numerical optimization of injector hole arrangement for marine methanol/diesel direct dual fuel stratification engines. *Appl. Therm. Eng.* **2024**, *257*, 124456. [CrossRef]
5. Huang, Q.; Yang, R.; Liu, J.; Xie, T.; Liu, J. Investigation of the mechanism behind the surge in nitrogen dioxide emissions in engines transitioning from pure diesel operation to methanol/diesel dual-fuel operation. *Fuel Process. Technol.* **2024**, *264*, 108131. [CrossRef]
6. Yang, R.; Shang, T.; Li, L.; Liu, J.; Xie, T.; Liu, Z.; Liu, J. The mechanism of the increased ratio of nitrogen dioxide to nitrogen oxides in methanol/diesel dual fuel engines. *Energy* **2024**, *312*, 133701. [CrossRef]
7. Li, Y.; Cai, Y.; Jia, M.; Wang, Y.; Su, X.; Li, L. A full-parameter computational optimization of both injection parameters and injector layouts for a methanol/diesel dual-fuel direct injection compression ignition engine. *Fuel* **2024**, *369*, 131733. [CrossRef]
8. Verhelst, S.; Turner, J.W.G.; Sileghem, L.; Vancoillie, J. Methanol as a fuel for internal combustion engines. *Prog. Energy Combust. Sci.* **2019**, *70*, 43–88. [CrossRef]
9. Wang, X.; Chang, X.; Liu, J.; Gao, J.; Wu, J.; He, H. Experimental investigation of high-pressure methanol spray characteristics for engines. *Appl. Therm. Eng.* **2025**, *271*, 126388. [CrossRef]
10. Wang, Y.; Dong, P.; Long, W.; Tian, J.; Wei, F.; Wang, Q.; Cui, Z.; Li, B. Characteristics of Evaporating Spray for Direct Injection Methanol Engine: Comparison between Methanol and Diesel Spray. *Processes* **2022**, *10*, 1132. [CrossRef]
11. Leng, X.; Xing, M.; Luo, Z.; Jin, Y.; He, Z.; Wei, S. An investigation on methanol high pressure spray characteristics and their predictive models. *Energy* **2024**, *313*, 133732. [CrossRef]
12. Zhang, Y.-J.; Wei, Y.-J.; Jamil, H.; Liu, S.-H. Investigation of the Behaviors of Methanol Spray Impingement and Wall Wetting. *Appl. Sci.* **2022**, *12*, 12263. [CrossRef]
13. Liu, K.; Chen, C.; Su, M.; Zhou, W.; Wang, Q.; Oppong, F.; Li, L.; Xu, C. Experimental study of the macroscopic characteristics of methanol low-pressure injection spray. *Int. J. Energy Res.* **2022**, *46*, 23259–23272. [CrossRef]
14. Li, X.; Xiang, L.; Wang, L.; Wang, Z.; Hu, Y. Experimental study on macroscopic and microscopic characteristics of flash boiling methanol spray under extremely cold conditions. *Energy Convers. Manag.* **2025**, *333*, 119780. [CrossRef]
15. Wu, F.; Yu, H.; Pan, X.; Zang, X.; Hua, M.; Wang, H.; Jiang, J. Experimental study of methanol atomization and spray explosion characteristic under negative pressure. *Process Saf. Environ. Prot.* **2022**, *161*, 162–174. [CrossRef]
16. Chen, Z.; Yao, A.; Yao, C.; Yin, Z.; Xu, H.; Geng, P.; Dou, Z.; Hu, J.; Wu, T.; Ma, M. Effect of fuel temperature on the methanol spray and nozzle internal flow. *Appl. Therm. Eng.* **2017**, *114*, 673–684. [CrossRef]

17. Wu, F.; Pan, X.; Wang, H.; Hua, M.; Yu, H.; Zang, X.; Jiang, J. Experimental study on the explosion characteristic and flame propagation of methanol spray at different injection pressures. *Fuel* **2022**, *325*, 124746. [CrossRef]
18. Cui, M.; Nour, M.; Fu, J.; Zhang, W.; Wang, G.; Xu, H.; Yao, B.; Li, X. Fundamental investigation of methanol flash boiling combustion under direct injection conditions. *Combust. Flame* **2025**, *276*, 114147. [CrossRef]
19. Chen, Z.; Zhao, P.; Wang, T.; He, H.; Chen, H.; Zhang, P.; Li, Y.; Geng, L.; Qi, D. Visualization study the cross spray and combustion characteristics of diesel and methanol in a constant volume combustion chamber at cold and flare flash boiling regions. *Energy* **2024**, *301*, 131654. [CrossRef]
20. Zhao, D.; An, Y.; Pei, Y.; Hu, J.; Hu, Z.; Zhang, Y. Optical study on spray mixing, flame propagation and jets evolution within visible methanol active pre-chamber for turbulent jet ignition. *Energy Convers. Manag.* **2024**, *319*, 118952. [CrossRef]
21. Pu, Y.-H.; Dierickx, J.; Verhelst, S. Modelling the evaporative cooling effect from methanol injection in the intake of internal combustion engines. *Fuel* **2024**, *372*, 132131. [CrossRef]
22. Sun, T.; Zhao, W.; Wang, T.; Liao, S.; Wei, H.; Zhou, L. Large-eddy simulation of methanol spray combustion characteristics in lean n-heptane mixture environments. *Fuel* **2026**, *405*, 136650. [CrossRef]
23. Otsu, N. A threshold selection method from gray-level histograms. *Automatica* **1975**, *11*, 23–27. [CrossRef]
24. Gaur, A.; Ailaboina, A.; Saha, K. Microscopic and macroscopic analysis of the flashing and non-flashing ethanol blended fuel for the direct injection sprays. *Appl. Therm. Eng.* **2025**, *260*, 124924. [CrossRef]
25. Amsden, A. *KIVA-II: A Computer Program for Chemically Reactive Flows with Sprays*; Los Alamos National Laboratory Report LA-11560-MS; Los Alamos National Laboratory (LANL): Los Alamos, NM, USA, 1989.
26. O'Rourke, P.J.; Amsden, A.A. A Spray/Wall Interaction Sub-Model for the KIVA-3 Wall Film Model. *SAE Trans.* **2000**, *109*, 281–298.
27. Han, Z.; Reitz, R.D. Turbulence Modeling of Internal Combustion Engines Using RNG κ-ε Models. *Combust. Sci. Technol.* **1995**, *106*, 267–295. [CrossRef]
28. Beale, J.C.; Reitz, R.D. Modeling spray atomization with the Kelvin-Helmholtz/Rayleigh-Taylor/hybrid model. *At. Sprays* **1999**, *9*, 623–650.
29. Schmidt, D.P.; Rutland, C.J. A new droplet collision algorithm. *J. Comput. Phys.* **2000**, *164*, 62–80. [CrossRef]
30. Zama, Y.; Ochiai, W.; Furuhata, T.; Arai, M. Experimental Study on Spray Angle and Velocity Distribution of Diesel Spray Under High Ambient Pressure Conditions. *At. Sprays* **2011**, *21*, 989–1007. [CrossRef]
31. Hiroyasu, H.; Kadota, T.; Arai, M. *Supplementary Comments: Fuel Spray Characterization in Diesel Engines*; Plenum Press: New York, NY, USA, 1980.
32. Chintagunti, S.J.; Agarwal, A.K. Effect of ambient pressure on macroscopic and microscopic spray characteristics of gasoline-diesel blends for gasoline compression ignition engine applications. *Appl. Energy* **2024**, *376*, 124106. [CrossRef]
33. Yanfeng, G.; Shenghua, L.; Yu, L. Investigation on methanol spray characteristics. *Energy Fuels* **2007**, *21*, 2991–2997. [CrossRef]
34. Delacourt, E.; Desmet, B.; Besson, B. Characterisation of very high pressure diesel sprays using digital imaging techniques. *Fuel* **2005**, *84*, 859–867. [CrossRef]
35. Payri, R.; García, A.; Domenech, V.; Durrett, R.; Plazas, A.H. An experimental study of gasoline effects on injection rate, momentum flux and spray characteristics using a common rail diesel injection system. *Fuel* **2012**, *97*, 390–399. [CrossRef]

Disclaimer/Publisher's Note: The statements, opinions and data contained in all publications are solely those of the individual author(s) and contributor(s) and not of MDPI and/or the editor(s). MDPI and/or the editor(s) disclaim responsibility for any injury to people or property resulting from any ideas, methods, instructions or products referred to in the content.